Received: 18 September 2024 | Revised: 4 December 2024 | Accepted: 14 December 2024

DOI: 10.1111/jace.20366

Journal of the American Ceramic Society

RESEARCH ARTICLE

Triple-point phase diagrams for BTO-based ceramics

David Gracia[1] | **François Fauth**[2] | **Sara Lafuerza**[1] | **Marco Evangelisti**[1] | **Javier Blasco**[1]

[1]Instituto de Nanociencia y Materiales de Aragón (INMA), CSIC-Universidad de Zaragoza, and Departamento de Física de la Materia Condensada, Universidad de Zaragoza, Zaragoza, Spain

[2]CELLS-ALBA Synchrotron Light Source, Cerdanyola del Vallès, Barcelona, Spain

Correspondence
David Gracia and Javier Blasco, Instituto de Nanociencia y Materiales de Aragón (INMA), CSIC-Universidad de Zaragoza, and Departamento de Física de la Materia Condensada, Universidad de Zaragoza, C/Pedro Cerbuna 12, 50009, Zaragoza, Spain.
Email: davidg@unizar.es and jbc@unizar.es

Funding information
ALBA Synchrotron, Grant/Award Number: 2023027380; Departamento de Educación, Cultura y Deporte, Gobierno de Aragón, Grant/Award Numbers: E11-23R, E12-23R; Ministerio de Ciencia, Innovación y Universidades, Grant/Award Numbers: CEX2023-001286-S, PID2021-124734OB-C21

Abstract

The temperature–composition structural phase diagram of the BTO-based ferroelectric system $Ba_{0.94}Ca_{0.06}Ti_{1-x}Hf_xO_3$ ($0.05 \leq x \leq 0.15$) is investigated using high-angular resolution synchrotron X-ray powder diffraction and dielectric permittivity measurements. In contrast to the well-known structural phase transition sequence of the parent compound $BaTiO_3$ (rhombohedral → orthorhombic → tetragonal → cubic, upon heating), Hf^{4+} doping into $Ba_{0.94}Ca_{0.06}Ti_{1-x}Hf_xO_3$ results in the gradual disappearance of the intermediate orthorhombic and tetragonal phases at two different, but close, critical concentrations, $0.10 < x_{c1} < 0.12$ and $0.12 < x_{c2} < 0.135$, respectively, revealing the presence of two triple points in the phase diagram.

KEYWORDS
barium titanate, dielectric constant, ferroelectricity/ferroelectric materials, X-ray methods

1 | INTRODUCTION

Lead-based piezoelectric ceramics, such as $PbTi_{1-x}Zr_xO_3$ (PZT), are regularly employed in commercial devices because of their good electromechanical properties and temperature stability.[1] Besides, among inorganic oxides these materials show the strongest electrocaloric effect (ECE), that is, the isothermal entropy ΔS_T and adiabatic temperature ΔT_{ad} changes following a change of the electric field.[2] This fact makes lead-based ceramics appealing for solid-state electrocaloric refrigeration, as recently demonstrated with a promising prototype.[3] However, lead is toxic and should be avoided in widespread applications. As piezoelectric and electrocaloric replacements, $BaTiO_3$ (BTO) and its derivatives are extensively investigated.[4,5]

BTO has a rich phase diagram. Above its Curie temperature T_c =393 K, it adopts the conventional cubic structure

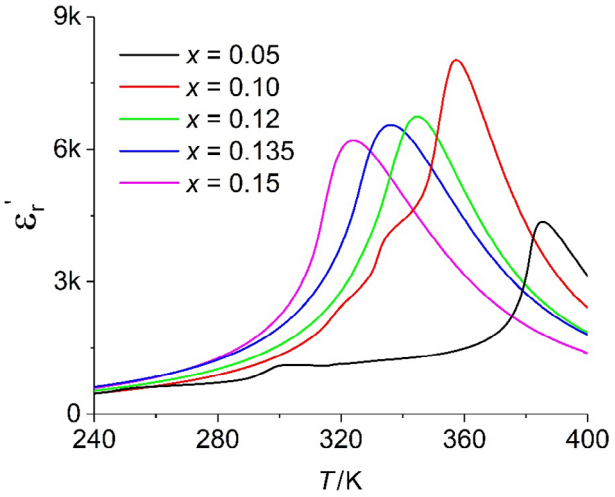

FIGURE 1 Temperature dependence of the real component of the dielectric permittivity for the different BCTH–x compositions in a selected temperature span.

of a perovskite (C phase, space group *Pm-3m*). Below T_c, BTO exhibits ferroelectricity and a tetragonal structure (T phase, space group *P4mm*), where the electric dipoles are aligned along the pseudocubic $(001)_c$ direction. Two more interferroelectric transitions take place at lower temperatures, yielding phases with different orientations of the electric dipoles. Below T_O =273 K, and above T_R =183 K, BTO is orthorhombic (O phase, space group *Amm2*) with the dipoles reoriented in the $(011)_c$ direction, and below T_R it adopts a rhombohedral structure (R phase, space group *R3m*), where the dipoles are oriented along the $(111)_c$ direction.[6,7]

Both electromechanical and electrocaloric properties are closely related to the occurrence of interferroelectric and ferroelectric–paraelectric phase transitions. The highest responses in the piezoelectricity of BTO-based ceramics are found near the morphotropic phase boundaries between the ferroelectric phases,[8] analogously to PZT. The ECE is usually maximized close to a ferroelectric–paraelectric phase transition.[9]

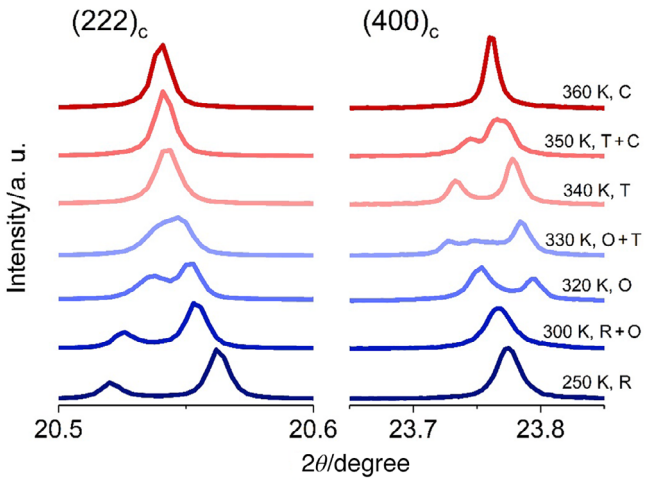

FIGURE 2 Evolution of the $(222)_c$ and $(400)_c$ reflections for BCTH-10 at selected temperatures. The structures employed in the Rietveld refinements are also indicated.

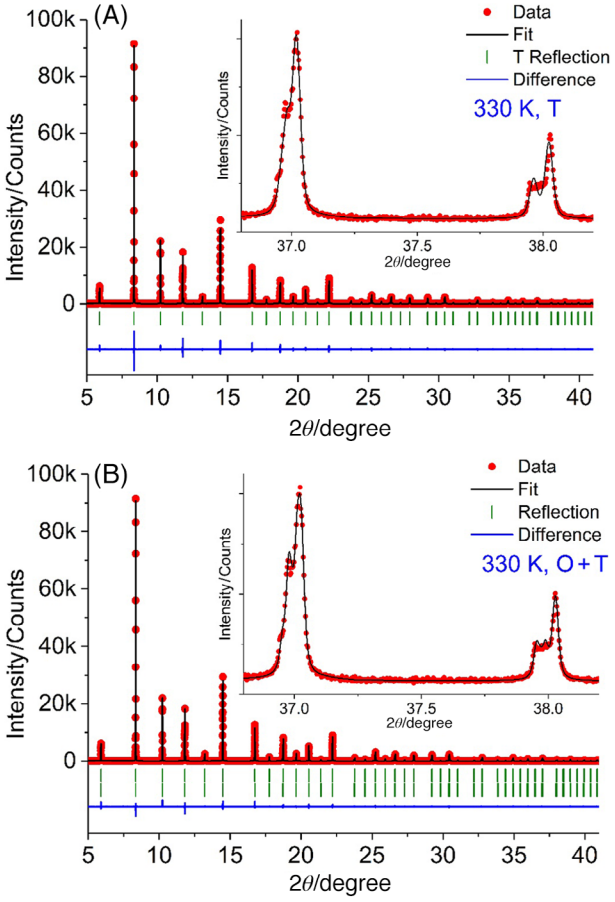

FIGURE 3 Best fits for BCTH-10 at 330 K, employing a single T structure (A) and a coexistence of O + T structures (B). The insets show the results for high angles, highlighting the improvement of the fit when a mixture of O + T phases is considered instead of a single T phase.

In BTO, the phase transitions can be tuned close to room temperature by isovalent substitutions in the Ba^{2+} and Ti^{4+} perovskite sites, therefore promoting large piezoelectric and electrocaloric responses at temperatures of interest for commercial applications. As an example, $Ba_{1-y}Ca_yTi_{1-x}M_xO_3$ (M = Sn, Zr, and Hf) solid solutions have been designed for enhanced piezoelectricity,[10–17] and ECE.[18–25] In these compositions, the isovalent Ca^{2+} substitution shifts T_O and T_R to lower temperatures, while with M^{4+} substitutions, T_O and T_R increase and T_c decreases. The three transitions eventually converge within a range of M^{4+} substitutions in the so-called phase convergence region, until a single ferroelectric–paraelectric R–C transition is observed.[4] Compositions close to the phase conver-

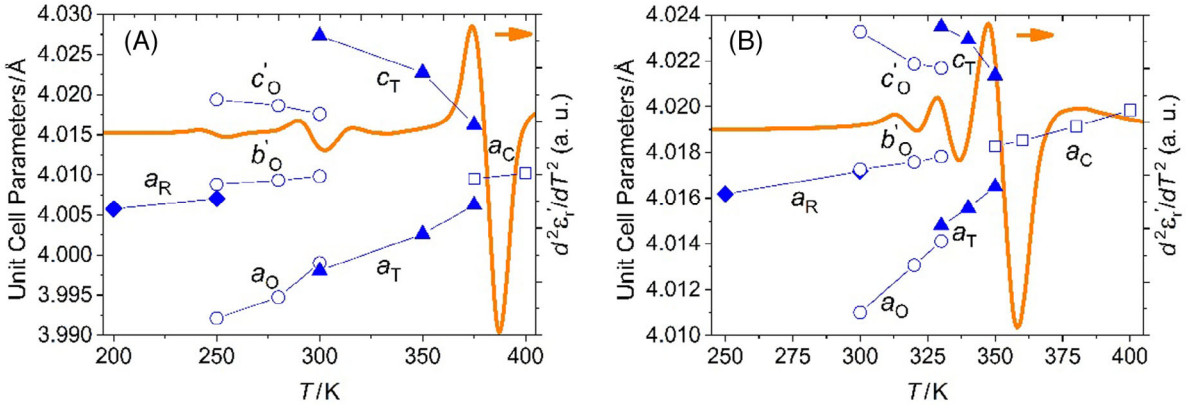

FIGURE 4 Unit cell parameters (symbols) and second derivative of the dielectric permittivity (solid line) for BCTH-05 (A) and BCTH-10 (B) as a function of the temperature. The standard deviations for the lattice parameters are smaller than the symbols sizes.

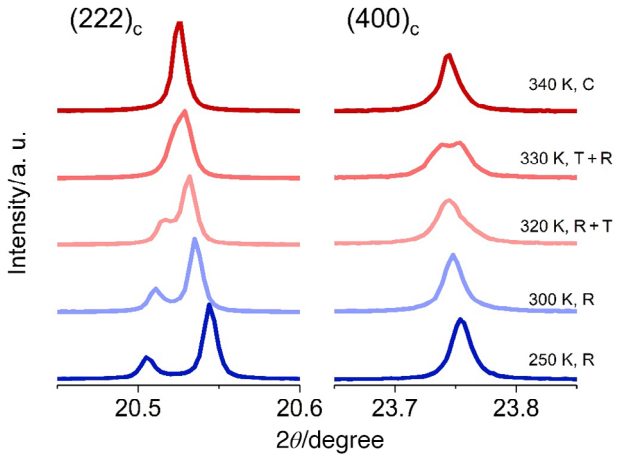

FIGURE 5 Evolution of the $(222)_c$ and $(400)_c$ reflections for BCTH-12 at selected temperatures. The structures employed in the Rietveld refinements are also indicated.

gence region are sought after since their electromechanical and electrocaloric properties can be enhanced thanks to all transitions merging within a narrow temperature span. Therefore, a precise knowledge of the different structural transitions is needed to understand and tune the relevant properties. However, the phase diagram of BTO-based solid solutions remains often controversial, as for instance for $Ba_{1-y}Ca_yTi_{1-x}Zr_xO_3$ (BCTZ). Some authors reported that, as the Zr^{4+} concentration increases, the O phase is present and acts as a structural bridge between the R–T phases, which are not group–subgroup related.[10–12,26] Eventually, this results in a phase convergence region where the R–O–T–C phases coexist in thermodynamic equilibrium. Contrarily, other studies reported that a mixture of R–T structures can be formed, without the O phase.[27–32]

In this work, we focus on the BTO-based ceramic $Ba_{0.94}Ca_{0.06}Ti_{1-x}Hf_xO_3$ because its phase convergence region occurs close to room temperature, resulting in appealing piezoelectric,[12,13] and electrocaloric properties.[18,19] Its behavior is expected to mimic other BTO-based solid solutions, such as BCTZ,[12,33] although no systematic structural characterization has been reported for this system. We employ high-angular resolution synchrotron X-ray powder diffraction (SXRPD) to distinguish the subtle distortions that give rise to the different structures around the phase convergence region, which cannot otherwise be resolved by conventional X-ray powder diffraction. We complement the structural study with dielectric permittivity measurements. Both characterizations point to the direction that a direct R–T transition occurs in a narrow interval of Hf^{4+} concentrations, leading to two triple points that are very close to each other in the composition–temperature phase diagram.

2 | EXPERIMENTAL PROCEDURES

A set of polycrystalline $Ba_{0.94}Ca_{0.06}Ti_{1-x}Hf_xO_3$ (BCTH–x) samples with $x = 0.05$, 0.10, 0.12, 0.135, and 0.15 were prepared mixing stoichiometric amounts of $BaCO_3$, $CaCO_3$, TiO_2, and HfO_2 by the conventional solid-state method. The weighted powders were initially heated at 1280°C for 3 h. The resulting mixtures were grounded and pressed into disk-shaped pellets (diameter of ~8 mm and thicknesses ~1.5 mm) and sintered for 48 h at 1450°C. As checked using conventional X-ray powder diffraction, this sintering process ensures that the samples are perfect solid solutions and well crystallized. Micrometric grain sizes are concluded from the absence of significant broadening in the diffraction peaks. Relative densities around 90% were obtained employing the Archimedes' method. These density values agree with previous studies in $BaTiO_3$ and are expected due to the high sintering temperature,[34] necessary to improve the grain coarsening.

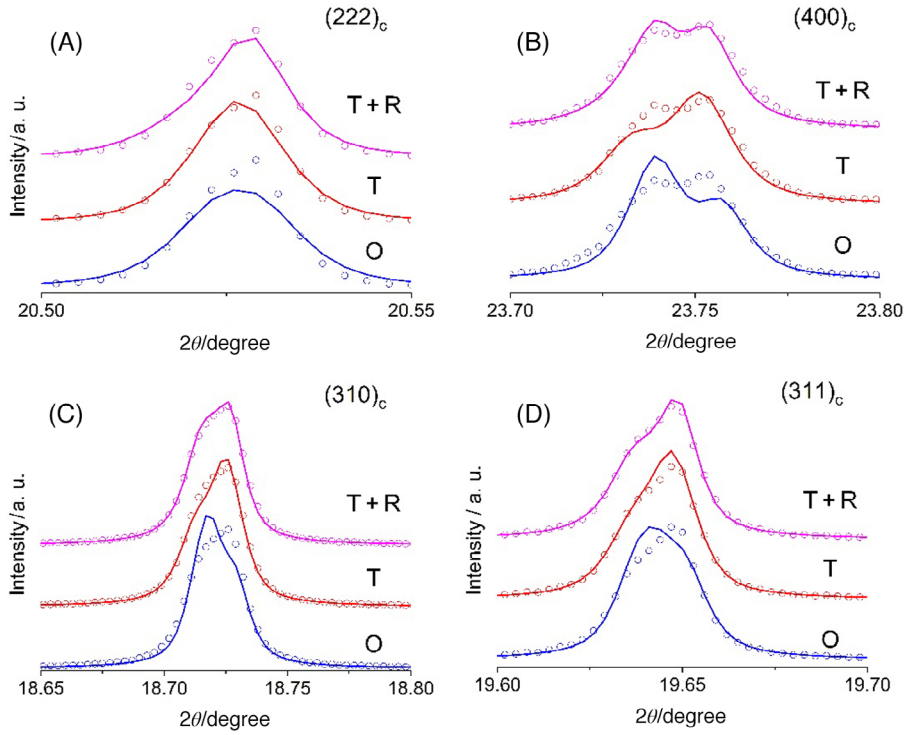

FIGURE 6 Best fits for the $(222)_c$ (A), $(400)_c$ (B), $(310)_c$ (C), and $(311)_c$ (D) reflections, using O, T, and T + R phases at 330 K for BCTH-12.

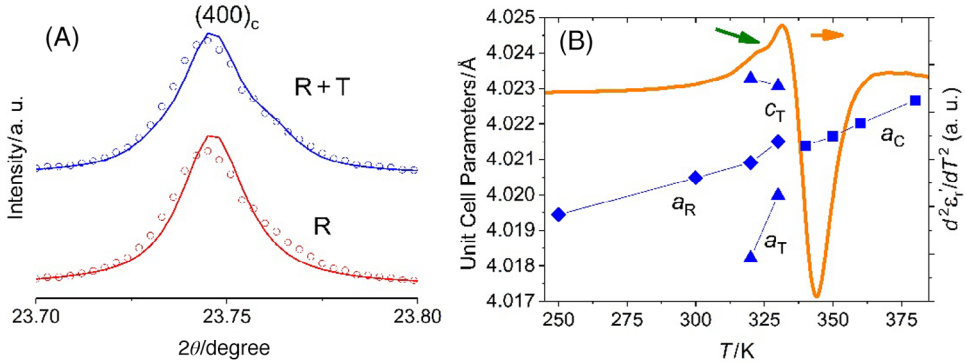

FIGURE 7 (A) Best fits for the $(400)_c$ reflection, using R and R + T phases at 320 K for BCTH-12. (B) Unit cell parameters (filled symbols) and second derivative of the dielectric permittivity (solid line) for BCTH-12 as a function of the temperature. The standard deviations for the lattice parameters are smaller than the symbols sizes. The green arrow indicates the position of the low-temperature anomaly in ε_r'.

SXRPD experiments were performed on the Material Science and Powder Diffraction (MSPD) beamline at the ALBA Synchrotron.[35] Sintered samples were grounded and a few milligrams were packed into a 0.5 mm capillary. The capillary was kept spinning during the data collection to improve powder averaging. The patterns were collected with photons of wavelength $\lambda = 0.41368$ Å in the 2θ range from 0.5° to 41° with steps of 0.005° using the Multi Analyzer Detection setup offering the highest achievable instrumental angular resolution.[36] A National Institute of Standards and Technology (NIST) standard silicon was used to calibrate the value of λ and the instrumental resolution. Samples were measured sequentially, one after the other, in the temperature range from 180 K to 430 K using an Oxford Cryostream 700+ model. The patterns were collected at constant temperature, after stabilizing the setup for 5 min. Heating ramps of 3 K min^{-1} were employed between the different temperature points.

Rietveld refinements were performed using the FullProf program.[37] The refined parameters included the 2θ offset, lattice parameters, atomic positions,

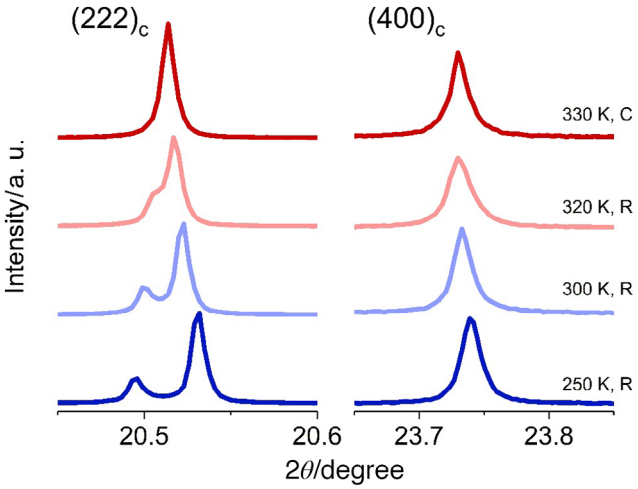

FIGURE 8 Evolution of the $(222)_c$ and $(400)_c$ reflections for BCTH-13.5 at selected temperatures. The structures employed in the Rietveld refinements are also indicated.

isotropic Debye–Waller factors, and background points. The Thompson–Cox–Hastings pseudo-Voigt function was employed including the Stephens' formalism for accounting anisotropic microstrain,[38] which leads to an anisotropic broadening of diffraction peaks that appeared to be significant in related systems, and it is necessary for accounting the complete profile of the peaks.[39] When a coexistence of two phases was found, for the minority phase, atomic positions and isotropic Debye–Waller factors were fixed to the values obtained at the closest available temperature to avoid high correlation of the refined parameters leading to unphysical results. The phase fractions were determined using standard Rietveld refinement techniques, as implemented by the FullProf program. The crystal systems were first identified based on the peak splitting of the $(hhh)_c$ and $(h00)_c$ pseudocubic reflections. In the high-temperature C phase, both types of reflections are single peaks. In the T phase, the $(hhh)_c$ reflections continue as single peaks but the $(h00)_c$ ones are split, while in the O phase both kinds of reflections are split. Finally, in the R phase $(hhh)_c$ remains split but $(h00)_c$ are single peaks. This evolution was checked measuring BTO as a reference (see Figure S1A). The initial assignments were confirmed by Rietveld refinements of the patterns achieving very good reliability factors. Examples of Rietveld refinements together with the refined parameters for all compositions can be consulted in the Supporting Information (Figures S2–S7 and Tables S1–S6).

The real component of the relative dielectric permittivity ε'_r of the samples was measured with an impedance analyzer 6500B (WayneKerr Electronics). The data were collected on heating ramps at 2 K min^{-1} in the temperature range from 180 K to 430 K, employing a liquid-nitrogen cryostat Optistat^{DN} (Oxford Instruments) and a home-made coaxial line insert. Sinusoidal excitations of 1 V amplitude and frequencies of 50 kHz were employed. Electrodes were made applying silver paste on the large surfaces of the disk-shaped samples. The temperature dependence of ε'_r for the different compositions is displayed in Figure 1. It can be appreciated that, as the Hf^{4+} content increases, the main peak associated with the ferroelectric–paraelectric phase transition shifts to lower temperatures, whereas the anomalies of the two secondary interferroelectric transitions move in the opposite direction until a single broad maximum is observed. In the following, the second derivative of ε'_r is employed instead to follow more clearly the temperature evolution of the different ferroelectric transitions.

3 | RESULTS AND DISCUSSION

3.1 | Transition sequence R–O–T–C

The two lowest Hf^{4+} content compositions, BCTH-05 and BCTH-10, showed the transition sequence R–O–T–C found in the parent compound BTO.[6,7] Figure 2 displays the dependence of the $(222)_c$ and $(400)_c$ reflections with the temperature for BCTH-10. An analogous peak splitting evolution was also found for BCTH-05 (see Figure S1B). The complete sequence of transitions was observed in both samples from the low-temperature ferroelectric R structure to the paraelectric C structure, including the O and T ferroelectric phases at intermediate temperatures.

Coexistences of two phases were also present close to the transition points. As an example, Figure 3 shows the Rietveld refinement at 330 K for BCTH-10. It is noticed that a mixture of O + T structures is required for fully explaining the pattern, while a single T phase alone is not able to account for the whole data. Furthermore, in some cases, such as for BCTH-05, diffuse scattering could be appreciated close to the transition temperatures because of the occurrence of nanodomains, that is, domains with small coherence length, of the minority phase (see Figure S1C).

The temperature dependence of the lattice parameters for both BCTH-05 and BCTH-10 is shown in Figure 4, together with the second derivative of the real component of the relative dielectric permittivity ε'_r for each sample. For the O structure, the parameters $b'_O = b_O/\sqrt{2}$ and $c'_O = c_O/\sqrt{2}$ are displayed instead.

The structural changes can be clearly appreciated with discontinuous jumps in the lattice parameters. In both

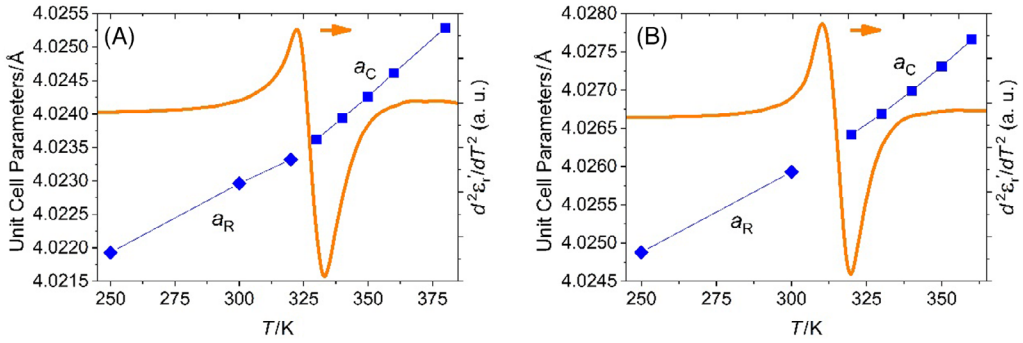

FIGURE 9 Unit cell parameters (filled symbols) and second derivative of the dielectric permittivity (solid line) for BCTH-13.5 (A) and BCTH-15 (B) as a function of the temperature. The standard deviations for the lattice parameters are smaller than the symbols sizes.

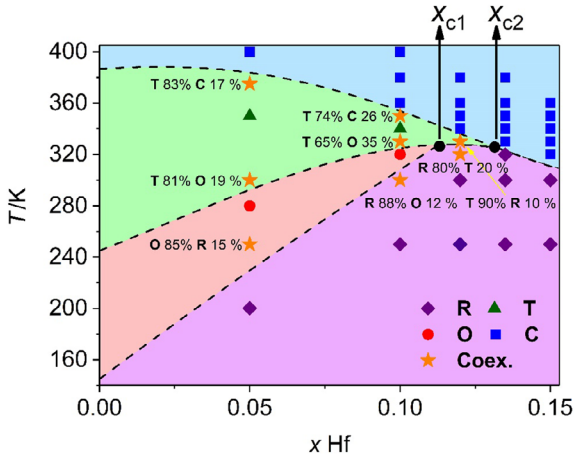

FIGURE 10 Proposed structural composition–temperature phase diagram based on the X-ray diffraction data. The dashed lines and the colored areas are guides to the eye. The two triple points are highlighted with black dots.

cases, the evolution is qualitatively similar to BTO,[6] although with different absolute values of the lattice parameters due to the smaller (larger) radii of Ca^{2+} (Hf^{4+}) when compared with Ba^{2+} (Ti^{4+}).[40] In the two samples, three anomalies are present in the second derivative of ε_r', matching well the temperature dependence of the structural transitions observed by powder X-ray diffraction. It is also clear that, the larger is the Hf^{4+} content, the narrower are the temperature ranges associated with the O and T phases. Rietveld refinements and refined structural parameters at selected temperatures for these two compositions can be consulted in the Supporting Information (Figures S3 and S4 and Tables S2 and S3).

3.2 | Transition sequence R–T–C

The composition with the intermediate Hf^{4+} content, BCTH-12, exhibited a temperature-dependent peak splitting for its $(222)_c$ and $(400)_c$ reflections represented in Figure 5. Up to 320 K, BCTH-12 presented a dominant rhombohedral structure, while above 340 K the structure of the sample agreed with the cubic paraelectric phase. In between, the data collected at 330 K points to an intermediate orthorhombic or tetragonal phase. The pattern seems to be almost single phase, with the $(400)_c$ peak split. Refinements to both T and O phases were tested. Examples of the fits obtained for both structures are depicted in Figure 6 for selected reflections.

The results of the fit to an O phase showed several problems. First, some unphysical parameters were obtained (negative isotropic Debye–Waller factors for oxygen atoms). Second, the intensity of some peaks was not well reproduced (see Figure 6A), while the profile of the split peaks showed intensities opposite to those obtained experimentally (see Figure 6B–D). Better reliability factors were also obtained in the fit to the T structure.

Additionally, the occurrence of minority phases can be appreciated at 320 K and 330 K. At 320 K, the R phase coexists with an additional phase as indicated by the broadening of the $(400)_c$ reflection at higher angles (Figure 5). First, an O phase was tried for the coexisting phase, but the results gave pseudotetragonal lattice parameters with $b'_O \approx a_O$ and far from a_R, strongly suggesting that the coexisting structure is tetragonal. Figure 7A illustrates the improvement of the profile refinement when a coexistence R + T is used instead of a pure R phase.

At 330 K, some small inaccuracy is still observed in some split peaks when only the T phase is considered (Figure 6). These small mismatches can be corrected by adding the contribution of a minority rhombohedral (pseudocubic) or cubic phase, as also shown in Figure 6 for the first case. It is very difficult to differentiate between the two possibilities since both refinements (either using a R or a C phase) gave similar reliability factors. We have opted for the R phase because a_R agrees better with the thermal evolution of the pseudocubic parameter in this sample, in

consistency with the trend observed for the rest of samples in this study, while a_C had a value close to c_T. Fits and refined data for this sample at several temperatures are reported in the Supporting Information (Figure S5 and Table S4).

Figure 7B shows the lattice parameters and the second derivative of the real component of the relative dielectric permittivity ε_r' dependence with the temperature. Only two anomalies can be spotted, the low temperature one being a subtle shoulder of the main peak and highlighted with a green arrow. This agrees with the powder X-ray diffraction data, where only two structural transitions identified as R–T and T–C were found. Therefore, both methods provide evidence that a direct R–T transition is occurring in BCTH–x without any intermediate O phase, as found experimentally also in BCTZ.[27–32] It can also be noted that in this composition the stability of the R phase extends to higher temperatures while the T phase begins to appear at slightly lower temperatures when compared with BCTH-10.

3.3 | Transition sequence R–C

For the compositions with the highest Hf^{4+} concentrations, BCTH-13.5 and BCTH-15, only a single transition between the ferroelectric R phase to the paraelectric C phase was observed in the diffraction data, as can be seen in Figure 8 for BCTH-13.5. The splitting of the $(222)_c$ reflection gradually decreases as the temperature raises, while the $(400)_c$ reflection remains as a single peak in the whole temperature range. The same behavior was observed for BCTH-15 (see Figure S1D). In both cases, no coexistence of the two phases was found in the studied temperature, suggesting that if such coexistence exists, it occurs in a very small temperature range (<10 K for BCTH-13.5). Rietveld refinements and structural data for these two compositions at representative temperatures are presented in the Supporting Information (Figures S6 and S7 and Tables S5 and S6).

As depicted in Figure 9, the temperature dependence of the lattice parameters for both compositions shows a smooth evolution without abrupt jumps when the R–C transitions take place, as like BCTZ for high Zr^{4+} concentrations.[41] By analogy with BCTZ, the continuous evolution points to a tricritical behavior, that is, a crossover between first- to second-order phase transition, once the phase convergence region is crossed.[42,43] Figure 9 also shows the second derivative of the real component of the relative dielectric permittivity ε_r' as a function of the temperature for both compositions, where only one broad anomaly is observed in the region where the structural R–C transition takes place.

3.4 | Phase diagram

The structural temperature–composition phase diagram based on the X-ray diffraction data is sketched in Figure 10, where structures or coexistences of structures refined for each composition are indicated. The dashed lines separating colored areas indicate approximately where a 50%–50% coexistence is expected for the different structural transitions. These lines are extended up to $x = 0$ using data from measurements reported elsewhere.[44]

At room temperature, BCTH–x crosses the O–T and R–O phase boundaries at concentrations of $x \approx 0.05$ and $x \approx 0.09$, respectively, in agreement with previous results.[12] Additionally, the disappearance of the intermediate O and T structures lies in values of Hf^{4+} concentrations close to previously reported results in BCTH–x from dielectric permittivity data.[12,18] However, in this work two triple points R–O–T and R–T–C were resolved very close to each other in composition, being the first in the Hf^{4+} concentration range $0.10 < x_{c1} < 0.12$ and the second in the Hf^{4+} concentration range $0.12 < x_{c2} < 0.135$, both at ~325 K. The second one is likely close to a tricritical point, which marks the boundary between first- and second-order transitions.

4 | CONCLUSIONS

Phase transitions of ferroelectric BCTH–x were investigated by high-angular resolution SXRPD and dielectric permittivity measurements. Both techniques evidenced that the full transition sequence R–O–T–C present in BTO is also found for low Hf^{4+} concentrations ($x < x_{c1}$), whereas only two transitions occurred for intermediate Hf^{4+} concentrations ($x_{c1} < x < x_{c2}$), namely, R–T and T–C. This behavior is consistent with the previously reported coexistence of rhombohedral and tetragonal phases in BCTZ,[27–32] and disagrees with the phase convergence region composed by the four phases.[10–12,26] For higher Hf^{4+} concentrations ($x > x_{c2}$), a single R–C transition was found. A temperature–composition phase diagram characterized by two triple points was presented based on the structural data inferred from Rietveld refinements. It is worth emphasizing that the presence of two triple points is completely consistent with the Gibbs phase rules for a pseudobinary phase diagram, unlike the coexistence of all four phases.[45]

Supporting Information. See the Supporting Information for the BTO, BCTH-05, and BCTH-15 peak splitting evolution with temperature and an example of diffuse scattering for BCTH-05 (Figure S1); examples of Rietveld refinements and refined structural parameters at selected temperatures for BTO (Figure S2 and Table S1); BCTH-05

(Figure S3 and Table S2); BCTH-10 (Figure S4 and Table S3); BCTH-12 (Figure S5 and Table S4); BCTH-13.5 (Figure S6 and Table S5); and BCTH-15 (Figure S7 and Table S6).

ACKNOWLEDGMENTS

This work was supported by MICIU/AEI/10.13039/501100011033 ERDF/UE (PID2021-124734OB-C21, CEX2023-001286-S), Gobierno de Aragón (E11-23R and E12-23R). David Gracia acknowledges financial support from the Gobierno de Aragón through a doctoral fellowship. We thank the Servicio General de Apoyo a la Investigación from the Universidad de Zaragoza. Granted beam time at ALBA Synchrotron is also acknowledged (Proposal No. 2023027380). We acknowledge support of the publication fee by the CSIC Open Access Publication Support Initiative through its Unit of Information Resources for Research (URICI).

ORCID

David Gracia https://orcid.org/0000-0002-3511-3510

REFERENCES

1. Lines ME, Glass AM. Principles and applications of ferroelectrics and related materials. New York: Oxford University Press; 1977.
2. Valant M. Electrocaloric materials for future solid-state refrigeration technologies. Prog Mater Sci. 2012;57:980. https://doi.org/10.1016/j.pmatsci.2012.02.001
3. Li J, Torelló A, Kovacova V, Prah U, Aravindhan A, Granzow T, et al. High cooling performance in a double-loop electrocaloric heat pump. Science. 2023;382:801. https://doi.org/10.1126/science.adi5477
4. Acosta M, Novak N, Rojas V, Patel S, Vaish R, Koruza J, et al. $BaTiO_3$-based piezoelectrics: fundamentals, current status, and perspectives. Appl Phys Rev. 2017;4:041305. https://doi.org/10.1063/1.4990046
5. Barman A, Kar-Narayan S, Mukherjee D. Caloric effects in perovskite oxides. Adv Mater Interfaces. 2019;6:1900291. https://doi.org/10.1002/admi.201900291
6. Kay HF, Vousden P. XCV symmetry changes in barium titanate at low temperatures and their relation to its ferroelectric properties. Lond Edinb Dub Phil Mag J. 1949;309:1900291. https://doi.org/10.1080/14786444908561371
7. Kwei GH, Lawson AC, Billinge SJL, Cheong SW. Structures of the ferroelectric phases of barium titanate. J Phys Chem. 1993;97:2368. https://doi.org/10.1021/j100112a043
8. Liu W, Ren X. Large piezoelectric effect in Pb-free ceramics. Phys Rev Lett. 2009;103:257602. https://doi.org/10.1103/PhysRevLett.103.257602
9. Moya X, Kar-Narayan S, Mathur ND. Caloric materials near ferroic phase transitions. Nat Mater. 2014;13:439. https://doi.org/10.1038/nmat3951
10. Zhang L, Zhang M, Wang L, Zhou C, Zhang Z, Yao Y, et al. Phase transitions and the piezoelectricity around morphotropic phase boundary in $Ba(Zr_{0.2}Ti_{0.8})O_3$-$x(Ba_{0.7}Ca_{0.3})TiO_3$ lead-free solid solution. Appl Phys Lett. 2014;105:162908. https://doi.org/10.1063/1.4899125
11. Tian Y, Wei L, Chao X, Liu Z, Yang Z. Phase transition behavior and large piezoelectricity near the morphotropic phase boundary of lead-free $(Ba_{0.85}Ca_{0.15})(Zr_{0.1}Ti_{0.9})O_3$ ceramics. J Am Ceram Soc. 2013;96:496. https://doi.org/10.1111/jace.12049
12. Zhao C, Wang H, Xiong J, Wu J. Composition-driven phase boundary and electrical properties in $(Ba_{0.94}Ca_{0.06})(Ti_{1-x}M_x)O_3$(M = Sn, Hf, Zr) lead-free ceramics. Dalton Trans. 2016;45:6466. https://doi.org/10.1039/C5DT04891E
13. Zhao C, Wu W, Wand H, Wu J. Site engineering and polarization characteristics $(Ba_{1-y}Ca_y)(Ti_{1-x}Hf_x)O_3$. J Appl Phys. 2016;119:024108. https://doi.org/10.1063/1.4939762
14. Zhao C, Feng Y, Wu H, Wu J. Phase boundary design and high piezoelectric activity in $(1-x)(Ba_{0.93}Ca_{0.07})TiO_3$-$xBa(Sn_{1-y}Hf_y)O_3$ lead-free ceramics. J Alloys Compd. 2016;666:372. https://doi.org/10.1016/j.jallcom.2016.01.105
15. Wang D, Jiang Z, Yang B, Zhang S, Zhang M, Guo F, et al. Phase transition behavior and high piezoelectric properties in lead-free $BaTiO_3$-$CaTiO_3$-$BaHfO_3$ ceramics. J Mater Sci. 2014;49:62. https://doi.org/10.1007/s10853-013-7650-9
16. Zhou C, Liu W, Xue D, Ren X, Bao H, Gao J, et al. Triple-point-type morphotropic phase boundary based large piezoelectric Pb-free material-$Ba(Ti_{0.8}Hf_{0.2})O_3$-$(Ba_{0.7}Ca_{0.3})TiO_3$. Appl Phys Lett. 2012;100:222910. https://doi.org/10.1063/1.4724216
17. Yao Y, Zhou C, Lv D, Wang D, Wu H, Yang Y, et al. Large piezoelectricity and dielectric permittivity in $BaTiO_3$-$xBaSnO_3$ system: the role of phase coexisting. EPL. 2012;98:27008. https://doi.org/10.1209/0295-5075/98/27008
18. Gracia D, Lafuerza S, Blasco J, Evangelisti M. The electrocaloric effect of lead-free $Ba_{1-y}Ca_yTi_{1-x}Hf_xO_3$ from direct and indirect measurements. APL Mater. 2023;11:121101. https://doi.org/10.1063/5.0173585
19. Wu P, Lou X, Li J, Li T, Gao H, Wu M, et al. Direct and indirect measurement of electrocaloric effect in lead-free $(100-x)Ba(Hf_{0.2}Ti_{0.8})O_3$-$x(Ba_{0.7}Ca_{0.3})TiO_3$ ceramics near multi-phase boundary. J Alloys Compd. 2017;725:275. https://doi.org/10.1016/j.jallcom.2017.07.103
20. Qian XS, Ye HJ, Zhang YT, Gu H, Li X, Randall CA, et al. Giant electrocaloric response over a broad temperature range in modified $BaTiO_3$ ceramics. Adv Funct Mater. 2014;24:1300. https://doi.org/10.1002/adfm.201302386
21. Li J, Zhang D, Qin S, Li T, Wu M, Wang D, et al. Large room temperature electrocaloric effect in lead-free $BaHf_{1-x}Ti_xO_3$ ceramics under low electric field. Acta Mater. 2016;115:58. https://doi.org/10.1016/j.actamat.2016.05.044
22. Sanlialp M, Luo Z, Shvartsman VV, Wei X, Liu Y, Dkhil B, et al. Direct measurement of electrocaloric effect in lead-free $Ba(Sn_xTi_{1-x})O_3$ ceramics. Appl Phys Lett. 2017;111:173903. https://doi.org/10.1063/1.5001196
23. Sanlialp M, Shvartsman VV, Acosta M, Dkhil B, Lupascu DC. Strong electrocaloric effect in lead-free $0.65Ba(Zr_{0.2}Ti_{0.8})O_3$-$0.35(Ba_{0.7}Ca_{0.3})TiO_3$ ceramics obtained by direct measurements. Appl Phys Lett. 2015;106:062901. https://doi.org/10.1063/1.4907774
24. Sanlialp M, Shvartsman VV, Acosta M, Lupascu DC. Electrocaloric effect in $Ba(Zr,Ti)O_3$-$(Ba,Ca)TiO_3$ ceramics measured

directly. J Am Ceram Soc. 2016;99:4022. https://doi.org/10.1111/jace.14456

25. Singh G, Bhaumik I, Ganesamoorthy S, Bhatt R, Karnal AK, Tiwari VS, et al. Electro-caloric effect in $0.45BaZr_{0.2}Ti_{0.8}O_3$-$0.55Ba_{0.7}Ca_{0.3}TiO_3$ single crystal. Appl Phys Lett. 2013;102:082902. https://doi.org/10.1063/1.4793213
26. Keeble DS, Benabdallah F, Thomas PA, Maglione M, Kreisel J. Revised structural phase diagram of $(Ba_{0.7}Ca_{0.3}TiO_3)$-$(BaZr_{0.2}Ti_{0.8}O_3)$. Appl Phys Lett. 2013;102:092903. https://doi.org/10.1063/1.4793400
27. Silva JPB, Queirós EC, Tavares PB, Sekhar KC, Kamakshi K, Moreira JA, et al. Ferroelectric phase transitions studies in $0.5Ba(Zr_{0.2}Ti_{0.8})O_3$-$0.5(Ba_{0.7}Ca_{0.3})TiO_3$ ceramics. J Electroceram. 2015;35:135. https://doi.org/10.1007/s10832-015-0005-y
28. Ehmke MC, Ehrlich SN, Blendell JE, Bowman KJ. Phase coexistence and ferroelastic texture in high strain $(1-x)Ba(Zr_{0.2}Ti_{0.8})O_3$–$x(Ba_{0.7}Ca_{0.3})TiO_3$ piezoceramics. J Appl Phys. 2012;111:124110. https://doi.org/10.1063/1.4730342
29. Haugen AB, Forrester JS, Blendell JE, Damjanovic D, Li B, Bowman KJ, et al. Structure and phase transitions in $0.5(Ba_{0.7}Ca_{0.3}TiO_3)$–$0.5(BaZr_{0.2}Ti_{0.8}O_3)$ from 100 °C to 150 °C. J Appl Phys. 2013;113:014103. https://doi.org/10.1063/1.4772741
30. Gao J, Sue D, Wang Y, Wang D, Zhang L, Wu H, et al. Microstructure basis for strong piezoelectricity in Pb-free $Ba(Zr_{0.2}Ti_{0.8})O_3$-$(Ba_{0.7}Ca_{0.3})TiO_3$ ceramics. Appl Phys Lett. 2011;99:092901. https://doi.org/10.1063/1.3629784
31. Lu S, Xu Z, Su S, Zuo R. Temperature driven nano-domain evolution in lead-free $Ba(Zr_{0.2}Ti_{0.8})O_3$-$50(Ba_{0.7}Ca_{0.3})TiO_3$ piezoceramics. Appl Phys Lett. 2014;105:032903. https://doi.org/10.1063/1.4891756
32. Gao J, Zhang L, Xue D, Kimoto T, Song M, Zhong L, et al. Symmetry determination on Pb-free piezoceramic $0.5Ba(Zr_{0.2}Ti_{0.8})O_3$-$0.5(Ba_{0.7}Ca_{0.3})TiO_3$ using convergent beam electron diffraction method. J Appl Phys. 2014;115:054108. https://doi.org/10.1063/1.4864130
33. Payne WH, Tennery VJ. Dielectric and structural investigations of the system $BaTiO_3$-$BaHfO_3$. J Am Ceram Soc. 1965;48:413. https://doi.org/10.1111/j.1151-2916.1965.tb14779.x
34. Chaisan W, Yimnirun R, Ananta S. Two-stage sintering of barium titanate ceramic and resulting characteristics. Ferroelectrics. 2007;346:84. https://doi.org/10.1080/00150190601180380
35. Fauth F, Peral I, Popescu C, Knapp M. The new material science powder diffraction beamline at ALBA Synchrotron. Powder Diffr. 2013;28:S360. https://doi.org/10.1017/S0885715613000900
36. Fauth F, Boer R, Gil-Ortiz F, Popescu C, Vallcorba O, Peral I, et al. The crystallography stations at the ALBA Synchrotron. Eur Phys J Plus. 2015;130:160. https://doi.org/10.1140/epjp/i2015-15160-y
37. Rodríguez-Carvajal J. Recent advances in magnetic structure determination by neutron powder diffraction. Physica B. 1993;192:55. https://doi.org/10.1016/0921-4526(93)90108-I
38. Stephens PW. Phenomenological model of anisotropic peak broadening in powder diffraction. J Appl Crystallogr. 1999;32:281. https://doi.org/10.1107/S0021889898006001
39. Schönau KA, Schmitt LA, Knapp M, Fuess H, Eichel RA, Kungl H, et al. Nanodomain structure of $Pb[Zr_{1-x}Ti_x]O_3$ at its phase boundary: investigations from local to average structure. Phys Rev B. 2007;75:184117. https://link.aps.org/doi/10.1103/PhysRevB.75.184117
40. Shannon RD. Revised effective ionic radii and systematic studies if interatomic distance in halides and chalcogenides. Acta Cryst. 1976;32:751. https://doi.org/10.1107/S0567739476001551
41. Buscaglia V, Tripathi S, Petkov V, Dapiaggi M, Deluca M, Gajović A, et al. Average and local atomic-scale structure in $BaZr_xTi_{1-x}O_3$ (x = 0.10, 0.20, 0.40) ceramics by high-energy X-ray diffraction and Raman spectroscopy. J Phys Condens Matter. 2014;26:065901. https://doi.org/10.1088/0953-8984/26/6/065901
42. Gao J, Hu X, Wang Y, Liu Y, Zhang L, Ke X, et al. Understanding the mechanism of large dielectric response in Pb-free $(1-x)Ba(Zr_{0.2}Ti_{0.8})O_3-x(Ba_{0.7}Ca_{0.3})TiO_3$ ferroelectric ceramics. Acta Mater. 2017;125:177. https://doi.org/10.1016/j.actamat.2016.11.064
43. Gao J, Dai Y, Hu X, Ke X, Zhong L, Li S, et al. Phase transition behaviour near the triple point for Pb-free $(1-x)Ba(Zr_{0.2}Ti_{0.8})O_3-x(Ba_{0.7}Ca_{0.3})TiO_3$ piezoceramics. EPL. 2016;115:37001. https://dx.doi.org/10.1209/0295-5075/115/37001
44. Shu C, Reed D, Button TW. A phase diagram of $Ba_{1-x}Ca_xTiO_3$ (x = 0-0.30) piezoceramics by Raman spectroscopy. J Am Ceram Soc. 2018;101:2589. https://doi.org/10.1111/jace.15415
45. Tisza L. The thermodynamics of phase equilibrium. Ann Phys. 1961;13:1. https://doi.org/10.1016/0003-4916(61)90027-6

SUPPORTING INFORMATION

Additional supporting information can be found online in the Supporting Information section at the end of this article.

How to cite this article: Gracia D, Fauth F, Lafuerza S, Evangelisti M, Blasco J. Triple-point phase diagrams for BTO-based ceramics. J Am Ceram Soc. 2024;e20366. https://doi.org/10.1111/jace.20366